

Configurational and Dynamical Heterogeneity in Superionic $\text{Li}_{5.3}\text{PS}_{4.3}\text{Cl}_{1.7-x}\text{Br}_x$

Pengbo Wang, Sawankumar Patel, Haoyu Liu, Po-Hsiu Chien, Xuyong Feng, Lina Gao, Benjamin Chen, Jue Liu, and Yan-Yan Hu*

The correlation between lattice chemistry and cation migration in high-entropy Li^+ conductors is not fully understood due to challenges in characterizing anion disorder. To address this issue, argyrodite family of Li^+ conductors, which enables structural engineering of the anion lattice, is investigated. Specifically, new argyrodites, $\text{Li}_{5.3}\text{PS}_{4.3}\text{Cl}_{1.7-x}\text{Br}_x$ ($0 \leq x \leq 1.7$), with varying anion entropy are synthesized and X-ray diffraction, neutron scattering, and multinuclear high-resolution solid-state nuclear magnetic resonance (NMR) are used to determine the resulting structures. Ion and lattice dynamics are determined using variable-temperature multinuclear NMR relaxometry and maximum entropy method analysis of neutron scattering, aided by constrained ab initio molecular dynamics calculations. 15 atomic configurations of anion arrangements are identified, producing a wide range of local lattice dynamics. High entropy in the lattice structure, composition, and dynamics stabilize otherwise metastable Li-deficient structures and flatten the energy landscape for cation migration. This resulted in the highest room-temperature ionic conductivity of 26 mS cm^{-1} and a low activation energy of 0.155 eV realized in $\text{Li}_{5.3}\text{PS}_{4.3}\text{Cl}_{0.7}\text{Br}$, where anion disorder is maximized. This study sheds light on the complex structure–property relationships of high-entropy superionic conductors, highlighting the significance of heterogeneity in lattice dynamics.

1. Introduction

All-solid-state batteries offer a promising future for advanced electrochemical energy storage, featuring improved safety and high energy density.^[1,2] To achieve high power density demands

P. Wang, S. Patel, H. Liu, X. Feng, L. Gao, B. Chen, Y.-Y. Hu
Department of Chemistry and Biochemistry
Florida State University
Tallahassee, FL 32306, USA
E-mail: yhu@fsu.edu

P.-H. Chien, J. Liu
Neutron Scattering Division
Oak Ridge National Laboratory
Oak Ridge, TN 37830, USA

Y.-Y. Hu
Center of Interdisciplinary Magnetic Resonance
National High Magnetic Field Laboratory
Tallahassee, FL 32310, USA

 The ORCID identification number(s) for the author(s) of this article can be found under <https://doi.org/10.1002/adfm.202307954>

DOI: 10.1002/adfm.202307954

the use of solid electrolytes with fast ion conduction, and developing superionic conductors requires an in-depth fundamental understanding of the composition–structure–ion conduction correlations.

Recent studies on thiophosphate-based fast ion conductors have shown remarkable ionic conductivities.^[3–6] Among them, Li-argyrodites continue to attract attention,^[7–16] which have demonstrated room-temperature ionic conductivities $>20 \text{ mS cm}^{-1}$, superior to other superionic conductors. In addition, the flexibility of the anion structural framework affords new chemistry toward tunable ionic conductivities. Such structural characteristics stem from the labile exchange of sulfur and halogen anions over the Wyckoff 4a and 4d sites.^[15,17,18] The anion mixing affects site occupancies of neighboring Li^+ ions.^[7,19] More specifically, Li^+ can reside at T5 (Wyckoff 48 h) and T5a (Wyckoff 24 g) sites in $\text{Li}_6\text{PS}_5\text{I}$, while it can occupy the extra T2 (Wyckoff 48 h) sites in $\text{Li}_6\text{PS}_5\text{Br}$ and $\text{Li}_6\text{PS}_5\text{Cl}$.^[19] These intermediate T2 sites bridge Li-cages and facilitate inter-cage hops^[10,19,20] for long-range Li^+ diffusion.

Moreover, theoretical studies also predicted that T4 (Wyckoff 16e) sites could provide better connectivity of the cages,^[19] and Li^+ occupancy at these sites was experimentally confirmed in non-halide argyrodites $\text{Li}_{4+x}\text{Al}_x\text{Si}_{1-x}\text{S}_4$ and oxysulfide argyrodites $\text{Li}_{6.15}\text{Al}_{0.15}\text{Si}_{1.35}\text{S}_{6-x}\text{O}_x$.^[21,22]

Based on the unique structural flexibility of argyrodites, many attempts have been made to enhance Li^+ ion transport via structural engineering, including cation doping ($\text{Li}_{6+x}\text{P}_{1-x}\text{M}_x\text{S}_5$)^[16,23–25] and $\text{Li}_{6+x}\text{Sb}_{1-x}\text{M}_x\text{S}_5$ ($\text{M} = \text{Si/Ge}$) and anion doping ($\text{Li}_6\text{PS}_{5-x}\text{Se}_x(\text{Br/I})$)^[27,28] and $\text{Li}_{6-x}\text{PS}_{5-x}(\text{Cl/Br})_{1+x}$.^[7–9] Even though high ionic conductivity can be achieved by means of cation doping, the incorporation of redox-active elements (Si/Ge) often compromises electrochemical stability.^[29] Anion doping proves effective in enhancing ion transport without narrowing the electrochemical stability window.^[30] The underlying mechanisms of anion disorder-induced superionic behavior are not yet fully understood, particularly in complex high-entropy (high structural disorder) systems.^[31–33] To investigate the contributions of different structural disorder to ion conduction, we synthesized the $\text{Li}_{5.3}\text{PS}_{4.3}\text{Cl}_{1.7-x}\text{Br}_x$ series with a locked Li content.

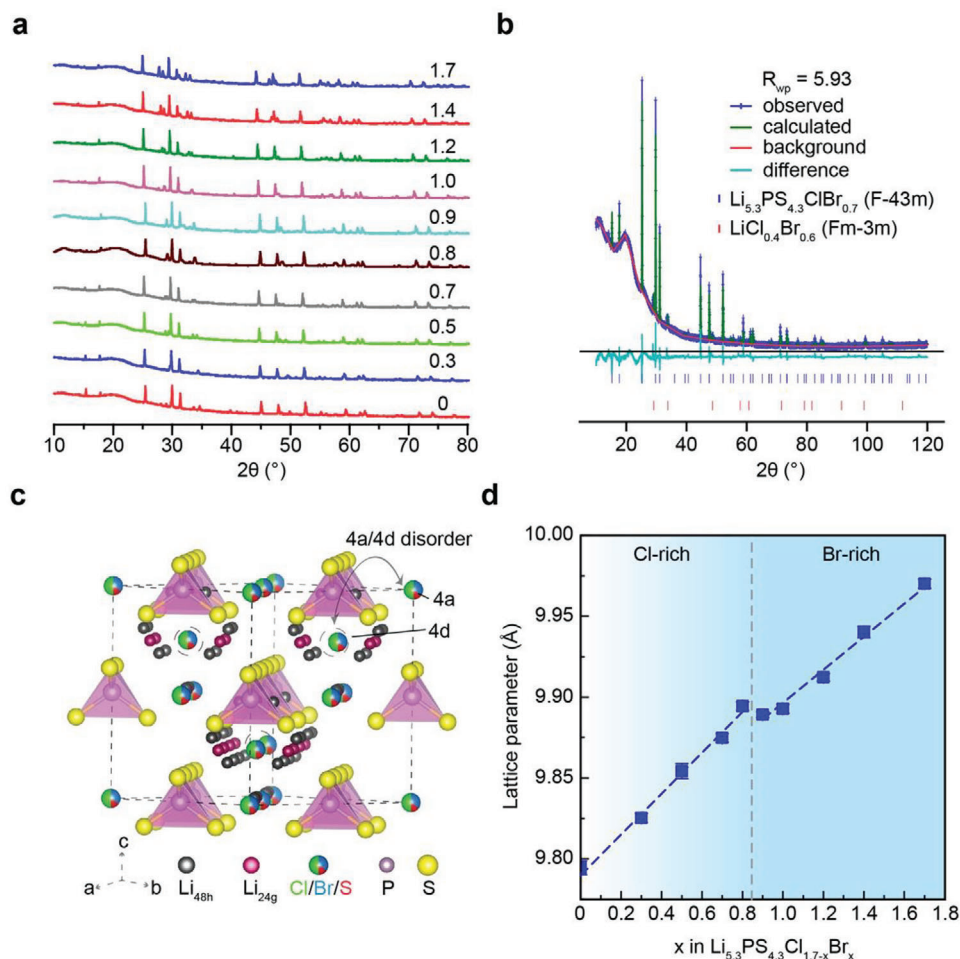


Figure 1. The long-range structures of $\text{Li}_{5.3}\text{PS}_{4.3}\text{Cl}_{1.7-x}\text{Br}_x$ determined with X-ray diffraction. a) Powder X-ray diffraction patterns of $\text{Li}_{5.3}\text{PS}_{4.3}\text{Cl}_{1.7-x}\text{Br}_x$ ($0 \leq x \leq 1.7$). b) Rietveld refinement of the diffraction pattern of $\text{Li}_{5.3}\text{PS}_{4.3}\text{ClBr}_{0.7}$. c) The crystal structure of $\text{Li}_{5.3}\text{PS}_{4.3}\text{ClBr}_{0.7}$, obtained from the Rietveld refinement. d) Lattice parameter as a function of x in $\text{Li}_{5.3}\text{PS}_{4.3}\text{Cl}_{1.7-x}\text{Br}_x$ ($0 \leq x \leq 1.7$). The discontinuity of the plot between $x = 0.8$ and 0.9 indicates significant structural adjustment when transitioning from Cl-rich to Br-rich compositions.

We achieved an unprecedented ionic conductivity of $\approx 26 \text{ mS cm}^{-1}$ in $\text{Li}_{5.3}\text{PS}_{4.3}\text{Cl}_{0.7}\text{Br}$, while maintaining nearly unchanged long-range structural order as determined by X-ray diffraction (XRD). However, atomic arrangements around active Li^+ ions exhibited high entropy as determined by multinuclear solid-state nuclear magnetic resonance (NMR). With NMR relaxometry and neutron scattering, we observed novel 4d-site configurations that contain S, Cl, and Br, and off-center 4a/4d positions, resulting in increased mobility of Li^+ ions and PS_4^{3-} polyhedra. The lattice dynamics strongly correlate with and contribute to enhanced Li^+ -ion transport, as revealed by constrained molecular dynamics simulations.

2. Results

The anion sublattice in argyrodite structures often exhibits site disorder between the divalent S^{2-} and monovalent halides (Br^- or Cl^-) at Wyckoff 4a and 4d positions. Moreover, the 4a/4d-site disorder is more prevalent between $\text{Cl}^-/\text{S}^{2-}$ than $\text{Br}^-/\text{S}^{2-}$ anions. For example, in $\text{Li}_6\text{PS}_5\text{X}$ ($\text{X} = \text{Cl}, \text{Br}$), the exchange between Cl^-

and S^{2-} at 4d sites is 63%, whereas for Br^- and S^{2-} is 43%.¹⁸ To study the influence of anion mixing on the structure and Li^+ conduction, we have synthesized and characterized a series of halogen-rich argyrodites $\text{Li}_{5.3}\text{PS}_{4.3}\text{Cl}_{1.7-x}\text{Br}_x$ ($0 \leq x \leq 1.7$). Our prior work showed that $\text{Li}_{5.3}\text{PS}_{4.3}\text{X}_{1.7}$ ($\text{X} = \text{Cl}$ or Br) formed stable phases with the largest Li deficiency and exhibited the highest ionic conductivities in respective mono-halide argyrodite series^[7,8]. The isovalent substitution of Cl^- with Br^- maintains constant lithium deficiency, thus allowing for isolating the effects of anion mixing on structure and ion conduction. Powder XRD is used to determine the long-range structural changes in halogen-rich argyrodites $\text{Li}_{5.3}\text{PS}_{4.3}\text{Cl}_{1.7-x}\text{Br}_x$. **Figure 1a** elucidates that the main phase of argyrodite (F-43m) is preserved in all $\text{Li}_{5.3}\text{PS}_{4.3}\text{Cl}_{1.7-x}\text{Br}_x$ ($0 \leq x \leq 1.7$) with a minor impurity phase $\text{LiCl}_{1-y}\text{Br}_y$ indexed to the rock salt structure (Fm-3m). The Cl/Br ratio in $\text{LiCl}_{1-y}\text{Br}_y$ is reflected in a linear variation of its lattice parameter (Figure S1b, Supporting Information), suggesting a solid-solution phase. Rietveld refinement is performed to determine the phase purity and the unit cell parameter for $\text{Li}_{5.3}\text{PS}_{4.3}\text{Cl}_{1.7-x}\text{Br}_x$. The Rietveld analysis on $\text{Li}_{5.3}\text{PS}_{4.3}\text{ClBr}_{0.7}$ is

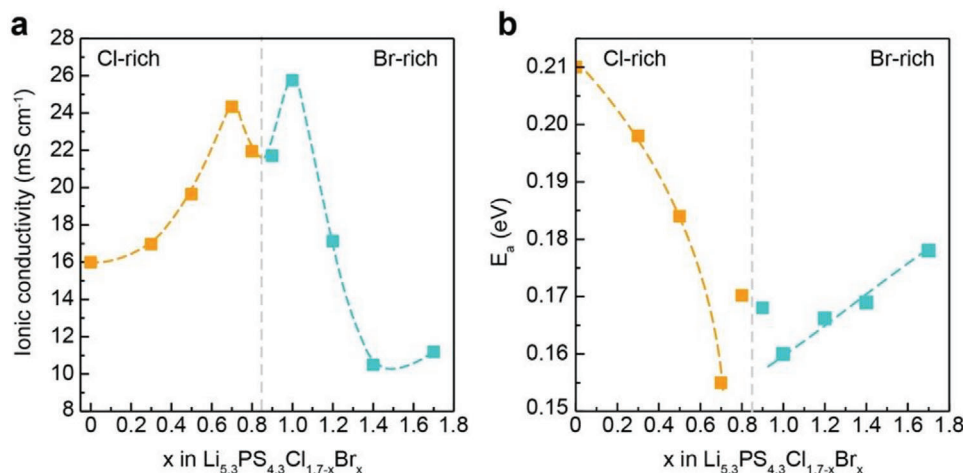


Figure 2. Ion conduction properties of $\text{Li}_{5.3}\text{PS}_{4.3}\text{Cl}_{1.7-x}\text{Br}_x$ ($0 \leq x \leq 1.7$). a) Room-temperature (25 °C) ionic conductivities determined with electrochemical impedance spectroscopy. Two maxima in conductivity, 24.3 and 25.7 mS cm^{-1} , are achieved when $x = 0.7$ and 1.0, respectively. b) Activation energy as a function of x in $\text{Li}_{5.3}\text{PS}_{4.3}\text{Cl}_{1.7-x}\text{Br}_x$ ($0 \leq x \leq 1.7$). The lowest activation energies in the Cl-rich ($x < 0.8$) and the Br-rich ($x > 0.9$) regions are 0.155 ($x = 0.7$) and 0.160 eV ($x = 1.0$), respectively.

shown in Figure 1b as an example, and the resulting structure is illustrated in Figure 1c. $\text{Li}_{5.3}\text{PS}_{4.3}\text{ClBr}_{0.7}$ is composed of 96.1 wt% of the argyrodite phase and 3.9 wt% of $\text{LiCl}_{0.6}\text{Br}_{0.4}$. The phase purity is high (>96%) in the middle of the series (Figure S1a, Supporting Information) between $x = 0.7$ –1.2, suggesting an unusual compositional space where the argyrodite structure is entropically stabilized by anion mixing. Bromination leads to a linear expansion of the unit cell (Figure 1d). The discontinuity in the linear pattern between $x = 0.8$ and 0.9 can be ascribed to nonuniform structural changes, supported by the irregular shifts of diffraction peaks at different angles as a function of x (Figure S1d, Supporting Information). The discontinuity separates the compositional space into distinct Cl-rich ($x = [0, 0.8]$) and Br-rich ($x = [0.9, 1.7]$) regions; these two regions exhibit contrasting structure-property correlations, as discussed below.

The ionic conductivities of $\text{Li}_{5.3}\text{PS}_{4.3}\text{Cl}_{1.7-x}\text{Br}_x$ are determined with electrochemical impedance spectroscopy (EIS). Figure 2a shows the room-temperature (25 °C) ionic conductivities calculated based on Nyquist plots of halogen-rich argyrodite $\text{Li}_{5.3}\text{PS}_{4.3}\text{Cl}_{1.7-x}\text{Br}_x$ (Figure S2, Supporting Information). Bromination of Cl-rich $\text{Li}_{5.3}\text{PS}_{4.3}\text{Cl}_{1.7-x}\text{Br}_x$ ($x < 0.8$) generally increases the ionic conductivity, and the highest conductivities for the Cl-rich and the Br-rich compositions are 24 and 26 mS cm^{-1} achieved with $x = 0.7$ ($\text{Li}_{5.3}\text{PS}_{4.3}\text{ClBr}_{0.7}$) and 1.0 ($\text{Li}_{5.3}\text{PS}_{4.3}\text{Cl}_{0.7}\text{Br}_{1.0}$), respectively. In the intermediate region ($x = 0.8$ and 0.9), a slight drop in ionic conductivity is observed. When the Br content becomes greater than 1, the conductivity declines rapidly. Figure 2b reveals that doping Br into the structure leads to lower activation energy in the Cl-rich side from $x = 0$ to 0.7, with the lowest value of 0.155 eV obtained for $x = 0.7$ ($\text{Li}_{5.3}\text{PS}_{4.3}\text{ClBr}_{0.7}$). Such a decrease in E_a originates from a softened lattice and increased disorder in the local structure when the relatively more polarizable Br replaces less polarizable Cl in the anion framework.^[15] However, on the Br-rich end, the change in E_a is smaller because the increase in Br content leads to a softer lattice but a more ordered structure, which has the opposite effects on the activation energy for ion transport.

To further probe the structure-ion conduction correlation in $\text{Li}_{5.3}\text{PS}_{4.3}\text{Cl}_{1.7-x}\text{Br}_x$, multinuclear high-resolution solid-state NMR is applied to determine structural disorder and ion dynamics. Similar to $\text{Li}_{6-x}\text{PS}_{5-x}\text{Br}_{1+x}$ and $\text{Li}_{6-x}\text{PS}_{5-x}\text{Cl}_{1+x}$,^{7,8} two ^6Li NMR resonances are observed, assigned to Li at 24 g and 48 h sites, respectively (Figure 3a). In the Cl-rich region ($x = [0, 0.8]$), with the increase in Br content, the ^6Li signal shifts toward a lower field, that is, larger ppm values (Figure 3b). From $x = 0.8$ to 0.9, the shift toward a higher field in the ^6Li resonances of $\text{Li}_{5.3}\text{PS}_{4.3}\text{Cl}_{1.7-x}\text{Br}_x$ signifies the onset of the transition from Cl-rich to Br-rich subseries. The Br-rich region ($x = [0.9, 1.7]$) exhibits smaller changes in the ^6Li resonance positions with respect to Br content compared with the Cl-rich region ($x = [0, 0.8]$). The observation from ^6Li NMR echoes the changes in the observed lattice parameter (Figure 1d). In the Cl-rich region ($x = [0, 0.8]$), the lattice expansion leads to reduced volumetric Li^+ density, often yielding the shifts of Li resonances to a lower field.^[7,8] When the argyrodite structure transitions from Cl-rich to Br-rich at $x = 0.8$ and 0.9,^[19] the shrinkage in the lattice parameter and Li-cages produces increased volumetric Li^+ density, thus resulting in the shifts of Li resonances to a higher field. In the Br-rich region ($x = [0.9, 1.7]$), the lattice parameter increases at a slow rate; thus ^6Li resonances shift toward the lower field again with a much smaller magnitude than in the Cl-rich region ($x = [0, 0.8]$). XRD and NMR consistently reveal the impact of $\text{Br} \rightarrow \text{Cl}$ replacement on average structural changes in $\text{Li}_{5.3}\text{PS}_{4.3}\text{Cl}_{1.7-x}\text{Br}_x$.

^6Li NMR further unveils changes of Li^+ site occupancy in $\text{Li}_{5.3}\text{PS}_{4.3}\text{Cl}_{1.7-x}\text{Br}_x$. The relative areal integrals of Li(24 g) and Li(48 h) ^6Li NMR resonances (Figure 3a) are quantitative measures of Li^+ site occupancies over 24 g and 48 h sites. Figure 3c shows the normalized fraction of Li (24 g) as a function of x in $\text{Li}_{5.3}\text{PS}_{4.3}\text{Cl}_{1.7-x}\text{Br}_x$. In our prior studies^[7,8], the 24 g sites in argyrodite structures constitute much of the Li^+ -ion transport pathways, and Li occupancy at 24 g sites is closely correlated with the observed ionic conductivity. Similarly, in $\text{Li}_{5.3}\text{PS}_{4.3}\text{Cl}_{1.7-x}\text{Br}_x$, the trend of conductivity is in accordance with that of Li (24 g) fraction, showing two maxima at $x = 0.7$ and 1.0. The slight

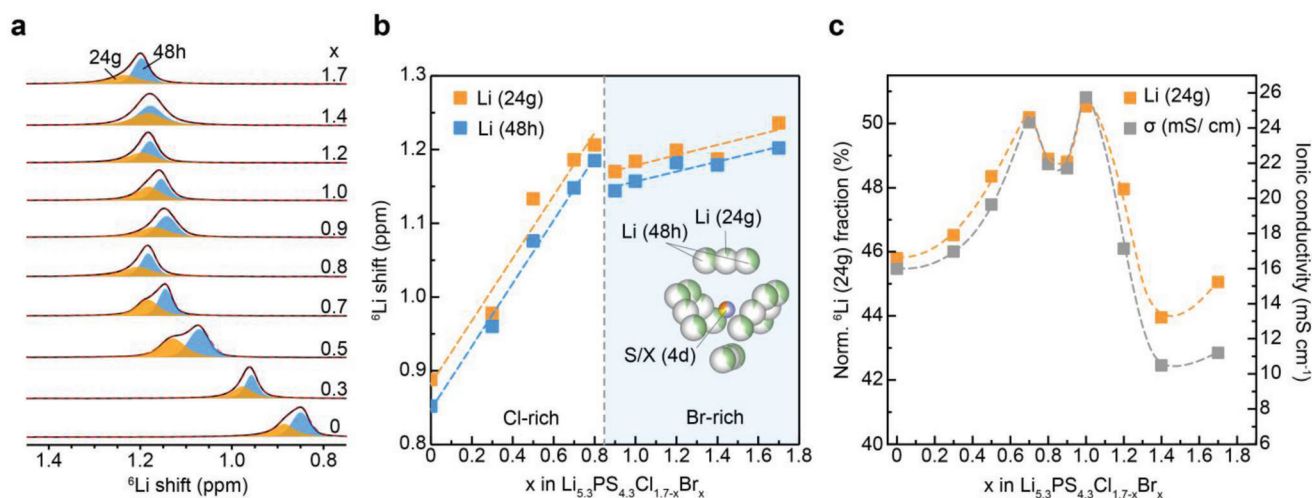


Figure 3. Li site occupancies in $\text{Li}_{5.3}\text{PS}_{4.3}\text{Cl}_{1.7-x}\text{Br}_x$ ($0 \leq x \leq 1.7$), determined with ^6Li magic-angle-spinning (MAS) NMR. a) ^6Li NMR spectra of $\text{Li}_{5.3}\text{PS}_{4.3}\text{Cl}_{1.7-x}\text{Br}_x$ ($0 \leq x \leq 1.7$), the two resonances are attributed to Li at Wyckoff 24 g (orange) and 48 h (blue) sites, respectively. The Wyckoff 24 g and 48 h sites in the argyrodite structure are illustrated in Figure 1c. b) ^6Li NMR shifts of Li(24 g) and Li(48 h) in $\text{Li}_{5.3}\text{PS}_{4.3}\text{Cl}_{1.7-x}\text{Br}_x$ ($0 \leq x \leq 1.7$) as a function of x . The dashed line drawn near $x = 0.85$ separates the Cl-rich and the Br-rich regions. The inset displays the relative locations of Li(24 g) and Li(48 h) in the argyrodite structure. c) The fraction of Li residing at Wyckoff 24 g sites, based on the spectral areal integrals of the ^6Li NMR resonances shown in (a). The ionic conductivity of $\text{Li}_{5.3}\text{PS}_{4.3}\text{Cl}_{1.7-x}\text{Br}_x$ ($0 \leq x \leq 1.7$) as a function of x is shown for reference, which tracks the fraction of Li occupying Wyckoff 24 g sites.

deviation at $x = 1.7$ is due to the significant fraction of less conductive byproduct $\text{LiCl}_y\text{Br}_{1-y}$.

As the host of the active Li^+ cations, the anion sublattice often determines Li distribution and dynamics.^[7,20] To understand the origin of Li redistribution in $\text{Li}_{5.3}\text{PS}_{4.3}\text{Cl}_{1.7-x}\text{Br}_x$ and fast Li^+ conduction, interrogation of its anion sublattice is carried out with multinuclear ^{31}P , ^{35}Cl , and ^{79}Br NMR. ^{31}P NMR is a sensitive probe to uncover the local disorder within the anion sublattice induced by other anion species.^[7,8] As shown in **Figure 4a**, the complexity of the ^{31}P NMR spectra reveals the intricacy of the anion sublattice in $\text{Li}_{5.3}\text{PS}_{4.3}\text{Cl}_{1.7-x}\text{Br}_x$. The two-end members of the series- $\text{Li}_{5.3}\text{PS}_{4.3}\text{Cl}_{1.7}$ and $\text{Li}_{5.3}\text{PS}_{4.3}\text{Br}_{1.7}$ -show well-resolved ^{31}P resonances, attributed to different $n\text{S}(4-n)\text{X}$ combinations occupying 4d sites of the argyrodite structure.^[7] As expected, with anion mixing, the possibilities of $n\text{S}(4-n)\text{X}$ combinations occupying 4d sites increase (more X^- at 4d sites), especially in the middle of the $\text{Li}_{5.3}\text{PS}_{4.3}\text{Cl}_{1.7-x}\text{Br}_x$ series. The new ^{31}P resonances are attributed to PS_4^{3-} near 4d sites with configurations of 2S1Cl1Br, 1S1Cl2Br, 1S2Cl1Br, 3Cl1Br, 2Cl2Br, and 1Cl3Br. An overall increase in ^{31}P NMR shift is observed with increasing the Br content in $\text{Li}_{5.3}\text{PS}_{4.3}\text{Cl}_{1.7-x}\text{Br}_x$. Fifteen possible 4d-site configurations are found and their ^{31}P shifts are summarized in **Figure 4b**. It shows that all the peaks have the tendency to shift away from 0 ppm with increasing x in $\text{Li}_{5.3}\text{PS}_{4.3}\text{Cl}_{1.7-x}\text{Br}_x$. This change in the ^{31}P shift is greater at the Cl-rich side ($x \leq 0.8$) than the Br-rich region, which echoes the observations from XRD (**Figure 1b**) and ^6Li NMR (**Figure 3a**). The probability of different 4d site configurations is a result of statistical co-occupancy of S, Cl, and Br at 4d sites. Therefore, the probability calculation^[7] on $\text{Li}_{6-x}\text{PS}_{5-x}\text{Br}_{1+x}$ demonstrated in our previous work is adopted to understand the mixing of S/Cl/Br. The result (**Figure 4c**) shows that in the middle of the series, the fractions of S, Cl, and Br at 4d sites are close to their compositional quota, indicating maximum

site disorder in the anion frameworks, that is, no site occupancy preference over 4a/4d for S, Cl, and Br. **Figure 4d** reveals that the maximum fractions of 2S1Cl1Br, 1S2Cl1Br, and 1S1Cl2Br are reached at $x = 0.7$ to 0.8, 1.0 to 1.2, and 1.0, respectively, which again shows the $\text{Li}_{5.3}\text{PS}_{4.3}\text{Cl}_{1.7-x}\text{Br}_x$ ($x = [0.7, 1.2]$) exhibits the maximum anion mixing at 4d sites. The random distribution of S^{2-} , Cl^- , and Br^- over 4a/4d sites suggest a unique compositional space within $\text{Li}_{5.3}\text{PS}_{4.3}\text{Cl}_{1.7-x}\text{Br}_x$ ($x = [0.7, 1.2]$), within which the energy penalty for site exchange of anions is nearly zero,^[30] thus no preference in site occupancy is observed. This is further corroborated by experimental evidence from ^{35}Cl and ^{79}Br NMR.

^{35}Cl NMR is used to examine anion mixing by probing the local environments of Cl. ^{35}Cl (spin-3/2) NMR exhibits large quadrupolar coupling interactions for disordered structures, which causes significant spectral broadening and compromises spectral resolution. Three-quantum (3Q) magic-angle-spinning (MAS) NMR is employed to achieve high resolution by producing purely isotropic resonances along the F_1 dimension, unveiling chemically inequivalent sites.^[34] **Figure 5a** (right) shows the triple quantum magic-angle-spinning (3QMAS) ^{35}Cl NMR spectrum of $\text{Li}_{5.3}\text{PS}_{4.3}\text{Cl}_{0.8}\text{Br}_{0.9}$, and the cross sections extracted from the 2D spectra at the resonance positions indicated by the grey dashed lines are shown to the left. Projections of the 2D spectra are displayed on top and left, respectively. In particular, the projection on the left of the 2D spectrum is the isotropic spectrum free of effects from quadrupolar coupling interactions, which exhibits one broad resonance centered around -40 ppm and one sharp resonance at 11 ppm with a broad shoulder to its left. The red dashed line on the 2D spectrum denotes $C_Q = 0$; resonances appearing along the $C_Q = 0$ line have no quadrupolar coupling interactions, suggesting highly symmetric environments or fast motion on the order of MHz that averages out the quadrupolar coupling interactions; resonances below the $C_Q = 0$ line has

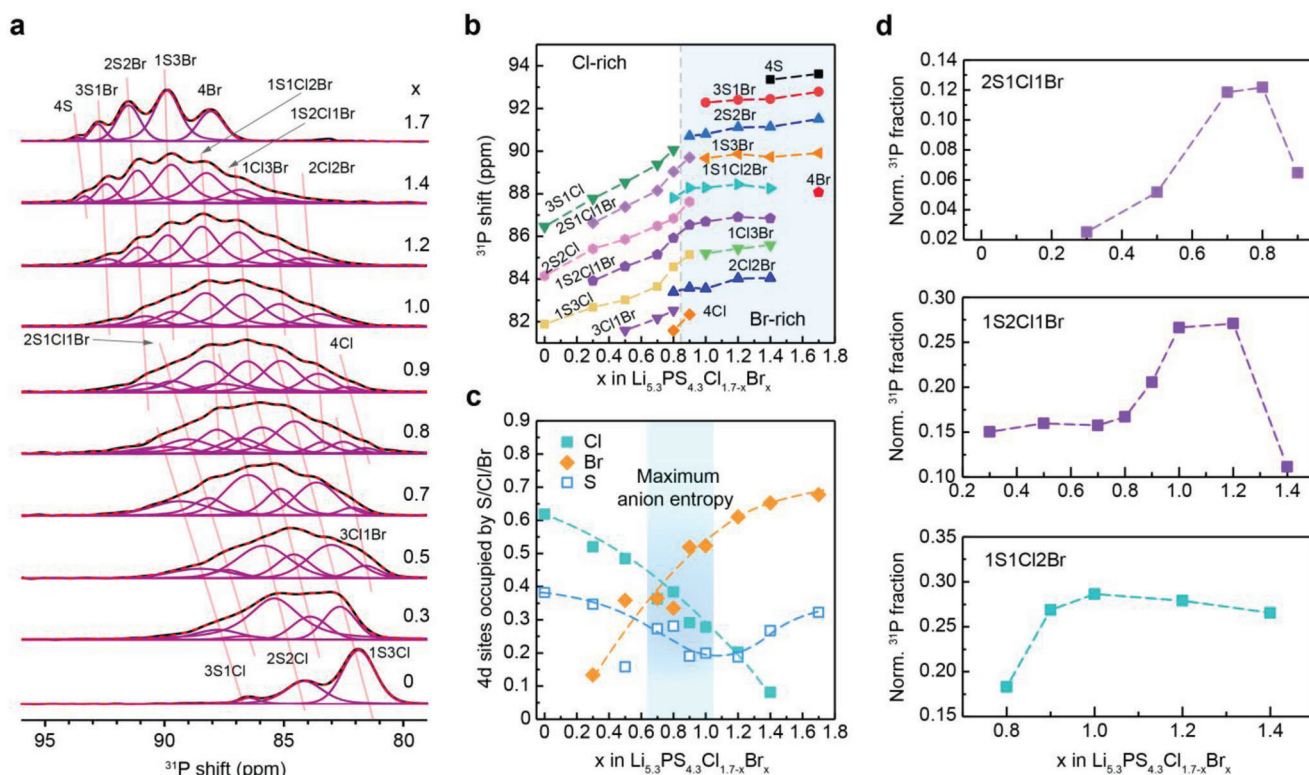


Figure 4. Anion entropy at Wyckoff 4d sites of $\text{Li}_{5.3}\text{PS}_{4.3}\text{Cl}_{1.7-x}\text{Br}_x$ ($0 \leq x \leq 1.7$) determined using high-resolution ^{31}P NMR. a) ^{31}P MAS NMR spectra of $\text{Li}_{5.3}\text{PS}_{4.3}\text{Cl}_{1.7-x}\text{Br}_x$. The Wyckoff 4d sites in the structure are near PS_4^{3-} units, thus ^{31}P NMR is very sensitive to changes of local structures at 4d-sites. Spectral analysis reveals 15 possible combinations of anions occupying the four Wyckoff 4d sites around PS_4^{3-} , that is, 4S, 3S1Br, 3S1Cl, 2S2Br, 2S2Cl, 2S1Cl1Br, 1S3Br, 1S3Cl, 1S1Cl2Br, 1S2Cl1Br, 4Br, 4Cl, 3Cl1Br, 2Cl2Br, and 1Cl3Br. b) ^{31}P NMR shifts of PS_4^{3-} associated with distinctive 4d-site configurations as a function of x in $\text{Li}_{5.3}\text{PS}_{4.3}\text{Cl}_{1.7-x}\text{Br}_x$. The perturbation to the local structure caused by Br-incorporation is more prominent in the Cl-rich region compared with that in the Br-rich region, consistent with lattice parameter changes shown in Figure 1 and ^6Li NMR in Figure 3. c) Fractions of the Wyckoff 4d sites occupied by Cl (cyan, filled square), Br (orange, filled rhombus), and S (blue, open square), respectively, in $\text{Li}_{5.3}\text{PS}_{4.3}\text{Cl}_{1.7-x}\text{Br}_x$ based on the analysis of the ^{31}P NMR spectra in (a). The highlighted area shows that the maximum anion entropy is found in $\text{Li}_{5.3}\text{PS}_{4.3}\text{Cl}_{1.7-x}\text{Br}_x$ with $0.7 \leq x \leq 1.0$, in which S, Cl, and Br nearly randomly distribute over 4d and 4a sites. d) Fractions of 4d configurations that contain all three elements S, Cl, and Br (from top to bottom: 2S1Cl1Br, 1S2Cl1Br, and 1S1Cl2Br) as a function of x in $\text{Li}_{5.3}\text{PS}_{4.3}\text{Cl}_{1.7-x}\text{Br}_x$.

non-vanishing quadrupolar coupling interactions. The ^{35}Cl resonance from the 4a sites is located close to the $C_Q = 0$ line but with a large breadth striding across the $C_Q = 0$ line, indicating that Cl_{4a} stays close to the highly symmetric center of the 4a sites. The significant broadening of the resonance is a result of fast relaxation (Figure S6 and Table S1, Supporting Information), likely induced by Cl^- ion dynamics. Cl_{4d} shows one sharp resonance and one broad shoulder, both of which locate below the $C_Q = 0$ line, suggesting non-vanishing C_Q induced by asymmetric local environments at the 4d sites. The sharp resonance closer to the $C_Q = 0$ line with a relatively smaller C_Q and slower relaxation (Figure S6 and Table S1, Supporting Information) is attributed to Cl at the center of 4d sites. While the broad shoulder with a faster relaxation ((Figure S6 and Table S1, Supporting Information)) is assigned to Cl at off-center 4d sites⁸; the cross-section taken at this resonance can be accurately simulated using the Czjzek model,^[35] suggesting a distribution of C_Q values generated as a result of a very disordered local environment.

To investigate the effect of bromination on Cl site occupancy, 1D ^{35}Cl NMR spectra of $\text{Li}_{5.3}\text{PS}_{4.3}\text{Cl}_{1.7-x}\text{Br}_x$ (Figure 5b) are acquired and analyzed based on the assignment from 2D 3QMAS

and T_1 results. It shows that Cl moves to off-center 4d sites when x is greater than 0.3 in $\text{Li}_{5.3}\text{PS}_{4.3}\text{Cl}_{1.7-x}\text{Br}_x$, suggesting that Br leads to the displacement of Cl. With more Cl located at off-center 4d sites upon bromination, Cl (off-center 4d)/Cl (4d) ratio reaches its maximum at $x = 1.0$ (Figure 5c). Figure S8a, Supporting Information, shows nearly no change in the position of the ^{35}Cl resonance for off-center 4d in the Br-rich region, which is consistent with the trends revealed by ^6Li (figure 3a) and ^{31}P (figure 4a) NMR. Figure 5d summarizes the fraction of 4d sites (including off-center sites) occupied by Cl, which decreases with increasing Br content, consistent with results obtained from ^{31}P NMR.

^{79}Br (spin-3/2) NMR is used to independently examine the local environments of Br in $\text{Li}_{5.3}\text{PS}_{4.3}\text{Cl}_{1.7-x}\text{Br}_x$. The broad range of ^{79}Br NMR shifts is further expanded by large quadrupolar interactions due to structural disorder. Thus, a quadrupolar Carr–Purcell–Meiboom–Gill (QCPMG) sequence is employed for broadband excitation with enhanced sensitivity. Br signals at 4d and 4a sites are resolved with characteristic powder patterns (Figure 6a).^[7] In addition, the ^{79}Br T_1 relaxation times of Br (4d) and Br (4a) in $\text{Li}_{5.3}\text{PS}_{4.3}\text{Cl}_{0.8}\text{Br}_{0.9}$ are determined as 42.5 and 24.1 ms, respectively (Figure S9, Supporting

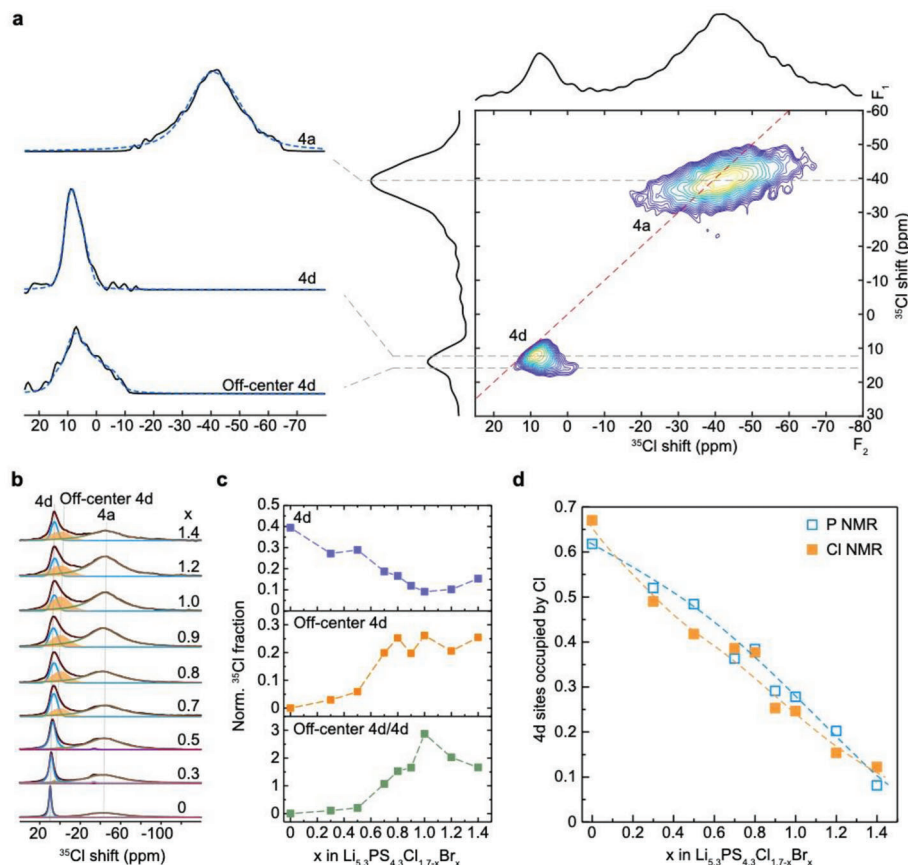


Figure 5. a) ^{35}Cl 3QMAS NMR spectrum of $\text{Li}_{5.3}\text{PS}_{4.3}\text{Cl}_{0.8}\text{Br}_{0.9}$. The red dashed line denotes $C_Q = 0$. Projections along the F_1 and F_2 dimensions are shown on the left and top of the 2D spectrum, respectively, where the projection along F_1 is the isotropic spectrum without effects from quadrupolar coupling interactions. Cross sections, displayed to the left of the 2D 3QMAS spectrum, are taken at the isotropic positions indicated by the grey dashed lines, corresponding to Cl occupying Wyckoff 4a, 4d, and off-center 4d sites. The simulated spectra (blue dashed lines) are superimposed with the extracted cross sections (black solid lines). b) ^{35}Cl MAS NMR spectra of $\text{Li}_{5.3}\text{PS}_{4.3}\text{Cl}_{1.7-x}\text{Br}_x$ ($0 \leq x \leq 1.4$). c) Quantitative analysis of the 1D ^{35}Cl NMR spectra of $\text{Li}_{5.3}\text{PS}_{4.3}\text{Cl}_{1.7-x}\text{Br}_x$ ($0 \leq x \leq 1.4$) shown in (b). The ratio of off-center 4d/4d reaches its maximum value when $x = 1.0$, manifesting that the effect of Br doping on the displacement of Cl is the greatest in $\text{Li}_{5.3}\text{PS}_{4.3}\text{Cl}_{0.7}\text{Br}$. d) Fractions of Cl occupying 4d sites (including off-center 4d) based on the analysis of ^{35}Cl spectra shown in (b), consistent with the values obtained from ^{31}P NMR shown in Figure 4, showing that the fraction of Cl occupying 4d sites decreases with increasing the Br content in $\text{Li}_{5.3}\text{PS}_{4.3}\text{Cl}_{1.7-x}\text{Br}_x$. Dashed lines are for guiding the eyes only.

Information); the distinct relaxation behavior allows spectral separation of Br (4d) and Br (4a) with high confidence. The ^{79}Br spectra of $\text{Li}_{5.3}\text{PS}_{4.3}\text{Cl}_{1.7-x}\text{Br}_x$ exhibit increased line width (Figure 6a) attributed to larger quadrupolar coupling interaction constants (C_Q) in the middle of the series (Figure S10, Supporting Information), indicating the lowering of local structural symmetry around Br. Semi-quantitative analysis on ^{79}Br NMR spectra shows that the fraction of 4d sites occupied by Br increases with Br content (Figure 6b), which echoes the trend from ^{31}P NMR.

The substitution of Br for Cl in $\text{Li}_{5.3}\text{PS}_{4.3}\text{Cl}_{1.7-x}\text{Br}_x$ also affects neighboring PS_4^{3-} reorientation motion. Maximum entropy method (MEM) analysis on neutron total scattering of $\text{Li}_{6-x}\text{PS}_{5-x}\text{ClBr}_x$ is used to examine the effect of bromination on PS_4^{3-} reorientation. Figure 7a shows the argyrodite structure of the (11-1) plane, which passes through Li and S atoms only. Since Li has a negative neutron scattering length, the positive scattering arises from S alone. Therefore, the distribution of nuclear density revealed from MEM plots can be used to analyze S delocalization and the associated motion of PS_4^{3-} . Figure 7b shows that the time-averaged S nuclear density is relatively localized in its origi-

nal positions within $\text{Li}_6\text{PS}_5\text{Cl}$, which suggests the limited motion of PS_4^{3-} . However, with increasing the Br content, the distribution of S nuclear density becomes more delocalized (Figure 7c,d), suggesting enhanced PS_4^{3-} reorientation. The PS_4^{3-} motion is also revealed by the S trajectories based on ab initio molecular dynamics (AIMD) simulations, which become more delocalized from $\text{Li}_6\text{PS}_5\text{Cl}$ (Figure 7e) to $\text{Li}_{5.25}\text{PS}_{4.25}\text{Cl}_{0.875}\text{Br}_{0.875}$ (Figure 7f). Therefore, increased Br content in $\text{Li}_{6-x}\text{PS}_{5-x}\text{ClBr}_x$ facilitates PS_4^{3-} reorientation motion.

To examine the PS_4^{3-} motional rate and its potential correlation with Li^+ transport in $\text{Li}_{6-x}\text{PS}_{5-x}\text{ClBr}_x$, NMR relaxometry is employed. According to the Bloembergen, Purcell, and Pound relaxation model, the relation between NMR T_1 relaxation and motion correlation time (τ_c), an indicator of mobility, can be described by

$$\left(\frac{1}{T_1}\right) = \frac{3\gamma^4\hbar^2}{10r_0^6} \left[\frac{\tau_c}{1 + \omega_0^2\tau_c^2} + \frac{4\tau_c}{1 + 4\omega_0^2\tau_c^2} \right] \quad (1)$$

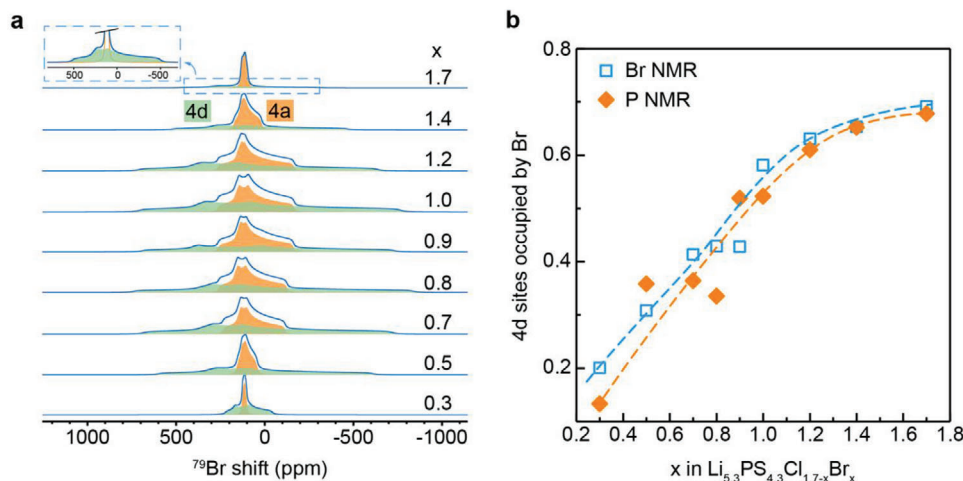


Figure 6. a) ^{79}Br static QCPMG NMR spectra of $\text{Li}_{5.3}\text{PS}_{4.3}\text{Cl}_{1.7-x}\text{Br}_x$ ($0.3 \leq x \leq 1.7$). ^{79}Br resonances from Br at the Wyckoff 4d and 4a sites are highlighted in green and orange, respectively. The increased line width of Br (4a) and Br (4d) between $x = 0.7$ and 1.2 signifies decreasing local symmetry around Br. b) Fractions of Br occupying 4d sites calculated based on the spectral areal integrals of ^{79}Br resonances shown in (a). It shows increased Br occupancy at 4d sites as increasing x in $\text{Li}_{5.3}\text{PS}_{4.3}\text{Cl}_{1.7-x}\text{Br}_x$ ($0.3 \leq x \leq 1.7$), which is in accordance with the information obtained from ^{31}P NMR. Equal Br occupancy at 4a and 4d sites occurs at $x = 1.0$.

where γ is the magnetogyric ratio, \hbar is the reduced Planck's constant, r_0 is the interatomic distance, and $\omega_0 = \gamma B_0$ is the Larmor frequency, and B_0 is the external magnetic field strength. When $\omega_0 \tau_c \ll 1$ (fast motional region), Equation (1) can be simplified to

$$\left(\frac{1}{T_1}\right) = \frac{3}{2} \frac{\gamma^4 \hbar^2}{r_0^6} \tau_c \quad (2)$$

which means that T_1 is proportional to τ_c^{-1} and field-independent; When $\omega_0 \tau_c \gg 1$ (slow motional region), Equation (1) can be approximated to

$$\left(\frac{1}{T_1}\right) = \frac{3}{5} \frac{\gamma^4 \hbar^2}{r_0^6} \frac{1}{\omega_0^2 \tau_c} \quad (3)$$

where T_1 is proportional to $\omega_0^2 \tau_c$ and thus field-dependent. Figure 7g shows a positive correlation of T_1 versus $T(K)$, thus T_1 increases with the motional rate ($\frac{1}{\tau_c}$) (Equation (2)), as $\tau_c(T)$ has an Arrhenius behavior.

$$\tau_c = \tau_{c,0} \exp\left(\frac{E_a}{kT}\right) \quad (4)$$

Therefore, PS_4^{3-} motion in $\text{Li}_{5.3}\text{PS}_{4.3}\text{Cl}_{0.7}\text{Br}$ falls in the fast-motion region where $\omega_0 \tau_c \ll 1$. This is also supported by weak field dependence of ^{31}P T_1 : the ratio of ^{31}P T_1 values measured at $\omega_0 = 336$ MHz versus 202 MHz is ≈ 1.1 for $\text{Li}_{5.3}\text{PS}_{4.3}\text{Cl}_{0.7}\text{Br}$ (Figure S12a, Supporting Information), implying that the field dependency is weak (Equation (2)). This value is around 1.1 ± 0.05 for all compositions (Figure S12a, Supporting Information), meaning that PS_4^{3-} motion of all $\text{Li}_{5.3}\text{PS}_{4.3}\text{Cl}_{1.7-x}\text{Br}_x$ is within the fast-motion region, where faster motion is indicated by larger T_1 values. Figure S12c, Supporting Information, shows that the maximum T_1 of $\text{Li}_{6-x}\text{PS}_{5-x}\text{ClBr}_x$ occurs within the range of $x = [1.0, 1.4]$, which confirms that the Br incorporation leads

to faster PS_4^{3-} reorientation, which agrees with the neutron diffraction and AIMD simulation results (Figure 7 a–f). To explore the origin of fast PS_4^{3-} reorientation in the compounds in $\text{Li}_{5.3}\text{PS}_{4.3}\text{Cl}_{1.7-x}\text{Br}_x$ for $x = [1.0, 1.4]$, the ^{31}P T_1 of P in different environments (Figure 4a) is closely examined. Figure 7h shows that the PS_4^{3-} surrounded by more halide ions and correspondingly fewer S ions in the second coordination shell exhibits longer T_1 , thus faster motions. Furthermore, Figure 7i shows mixed halogens result in faster PS_4^{3-} motion. Notably, the Wyckoff 4d-site configuration, 2Cl2Br, delivers the fastest PS_4^{3-} motion, and its fraction among all compositions is the highest in the range $x = [0.8, 1.0]$ (Figure S5, Supporting Information), indicating a possible correlation among X-anion site ordering, polyanion rotation, and Li^+ -ion conduction. Figure S13a–d, Supporting Information, summarizes the fractions of 4d-combinations (4X, 1S3X, 2S2X, and 3S1X, X = Cl/Br) as a function of x in $\text{Li}_{6-x}\text{PS}_{5-x}\text{ClBr}_x$. It shows that in the range of $x = [1.0, 1.4]$, the halogen-rich combinations, 4X (Figure S13a, Supporting Information) and 1S3X (Figure S13b, Supporting Information) are abundant, while the halogen-deficient combinations, 2S2X (Figure S13c, Supporting Information) and 3S1X (Figure S13d, Supporting Information) are scarce. Therefore, multiple ($n > 2$ for $(4-n)\text{SnX}$) halide ions at the local coordination sphere seem to facilitate the reorientation of neighboring PS_4^{3-} .

The interfaces between the Li and the S trajectories indicate potentially correlated motion of Li^+ and PS_4^{3-} (Figure 8a). To investigate the effects of PS_4^{3-} motion on Li^+ diffusion, mean square displacements (MSD) of Li in the $\text{Li}_{5.25}\text{PS}_{4.25}\text{Cl}_{0.875}\text{Br}_{0.875}$ structures with different anion dynamical constraints are calculated based on AIMD simulations. Without constraints, a high overall MSD is observed with nearly equal MSD in all three dimensions (Figure 8b). When the PS_4^{3-} units in the unit cell are immobilized, the overall Li MSD plummets to around half of the initial value (Figure 8c). The structure with all anions immobilized was investigated to include the effects from other anions, such as S^{2-} and X^- , which shows that the overall Li

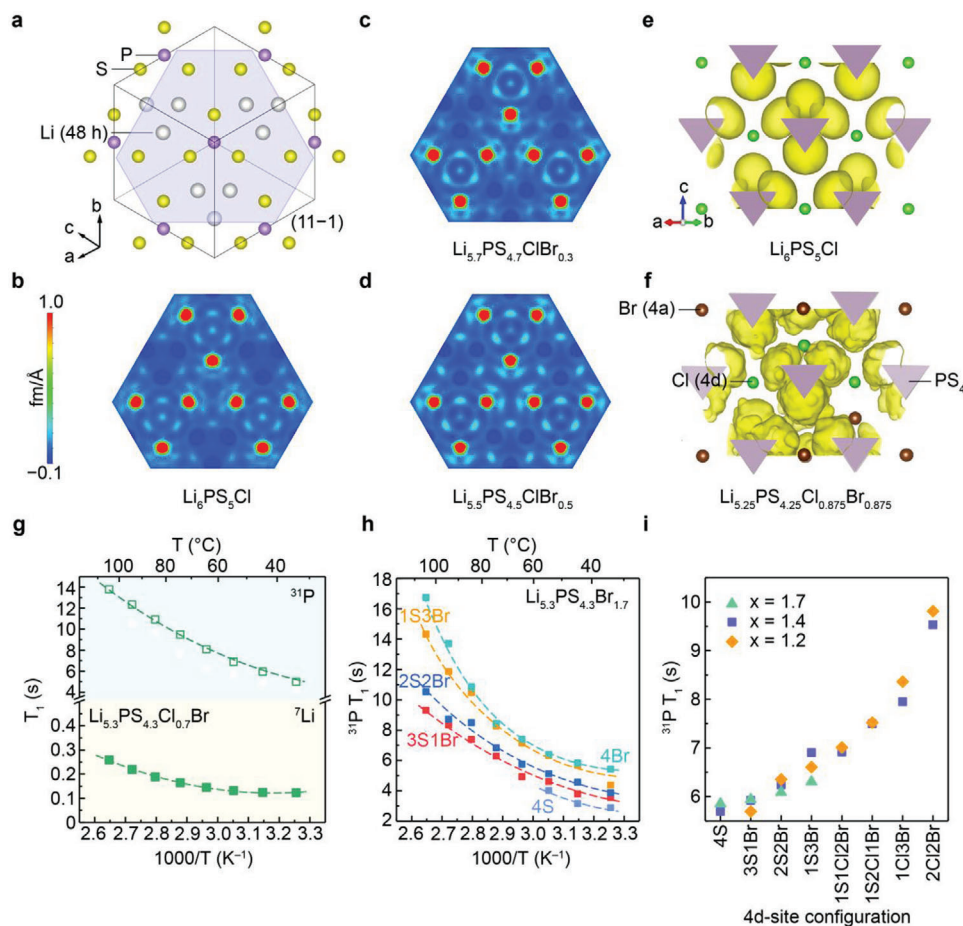


Figure 7. PS_4^{3-} motion in $\text{Li}_{5.3}\text{PS}_{4.3}\text{Cl}_{1.7-x}\text{Br}_x$ examined with neutron total scattering and NMR relaxometry. a) Crystal structure of argyrodite through the (11-1) plane. Element density maps of S generated based on the neutron total scattering of $\text{Li}_6\text{PS}_5\text{Cl}$ and $\text{Li}_{5.3}\text{PS}_{4.3}\text{Cl}_{1.7-x}\text{Br}_x$ for $x = 0, 0.3$, and 0.5 , using the maximum entropy method (MEM): b) $\text{Li}_6\text{PS}_5\text{Cl}$; c) $\text{Li}_{5.7}\text{PS}_{4.7}\text{ClBr}_{0.3}$; d) $\text{Li}_{5.5}\text{PS}_{4.5}\text{ClBr}_{0.5}$. Delocalized density of S across the plane qualitatively signifies PS_4^{3-} motion, which increases from $\text{Li}_6\text{PS}_5\text{Cl}$, to $\text{Li}_{5.7}\text{PS}_{4.7}\text{ClBr}_{0.3}$, and further to $\text{Li}_{5.5}\text{PS}_{4.5}\text{ClBr}_{0.5}$. AIMD simulations of S trajectories in e) $\text{Li}_6\text{PS}_5\text{Cl}$ and f) $\text{Li}_{5.25}\text{PS}_{4.25}\text{Cl}_{0.875}\text{Br}_{0.875}$. Delocalization of S manifests enhanced PS_4^{3-} motion in $\text{Li}_{5.25}\text{PS}_{4.25}\text{Cl}_{0.875}\text{Br}_{0.875}$ compared with $\text{Li}_6\text{PS}_5\text{Cl}$. g) ^{31}P and ^7Li NMR T_1 relaxation times as a function of temperature for $\text{Li}_{5.3}\text{PS}_{4.3}\text{Cl}_{0.7}\text{Br}$. The similar trend indicates that the motional rates of Li^+ and PS_4^{3-} are comparable on the timescale. h) Variable-temperature ^{31}P T_1 of the PS_4^{3-} units surrounded by different 4d-combinations (4S, 3S1Br, 2S2Br, 1S3Br, and 4Br) in $\text{Li}_{5.3}\text{PS}_{4.3}\text{Br}_{1.7}$. It indicates that the PS_4^{3-} motion increases with the Br content of the 4d-shell. i) ^{31}P T_1 of PS_4^{3-} in different 4d-combinations for $\text{Li}_{5.3}\text{PS}_{4.3}\text{Cl}_{1.7-x}\text{Br}_x$ ($x = 1.2, 1.4$, and 1.7). It reveals the heterogeneity of lattice dynamics and Cl/Br mixing facilitates PS_4^{3-} rotational motion.

MSD under this constraint is almost the same as the one with only PS_4^{3-} immobilized, implying that the anion motion of PS_4^{3-} bears dominant relevance to Li transport. To explore the relationship between Li^+ -ion conduction and anion motion from a different perspective, the MSD of $\text{Li}_6\text{PS}_5\text{Cl}$ is calculated (Figure S11c, Supporting Information), which is much smaller than that of $\text{Li}_{5.25}\text{PS}_{4.25}\text{Cl}_{0.875}\text{Br}_{0.875}$; this echoes with limited PS_4^{3-} motion determined with ^{31}P NMR T_1 ($\text{Li}_6\text{PS}_5\text{Cl}$: 3.98 s^{14} versus $\text{Li}_{5.3}\text{PS}_{4.3}\text{Cl}_{0.7}\text{Br}$: 4.5 s) and neutron scattering (Figure 7b).

3. Conclusion

In summary, we present new findings on argyrodite superionic conductors with compositions of $\text{Li}_{5.3}\text{PS}_{4.3}\text{Cl}_{1.7-x}\text{Br}_x$, which were synthesized to investigate the effects of anion entropy on Li^+ conduction. Our study systematically explores the impact of local an-

ion disorder on ionic conductivity, leading to the highest room-temperature ionic conductivity. Combining XRD, neutron scattering, and multinuclear solid-state NMR, we demonstrate the middle members of the $\text{Li}_{5.3}\text{PS}_{4.3}\text{Cl}_{1.7-x}\text{Br}_x$ series ($x = [0.7, 1.0]$) display the maximum anion disorder without significant changes in long-range structure. This high entropy of the anion sublattice is manifested by the random distribution of S, Cl, and Br over Wyckoff 4a/4d sites. We identify 15 atomic configurations of the Wyckoff 4d sites neighboring PS_4^{3-} polyhedra, which yield a wide range of PS_4^{3-} rotational motion as evidenced by both MEM analysis of neutron scattering and NMR relaxometry. The PS_4^{3-} rotational motion is on the same time scale as Li^+ motion, and constrained AIMD simulations suggest that such motion promotes Li^+ transport. Overall, the compositional, structural, and dynamical entropy in the anion sublattice stabilizes structures otherwise metastable and regulates cation transport by re-

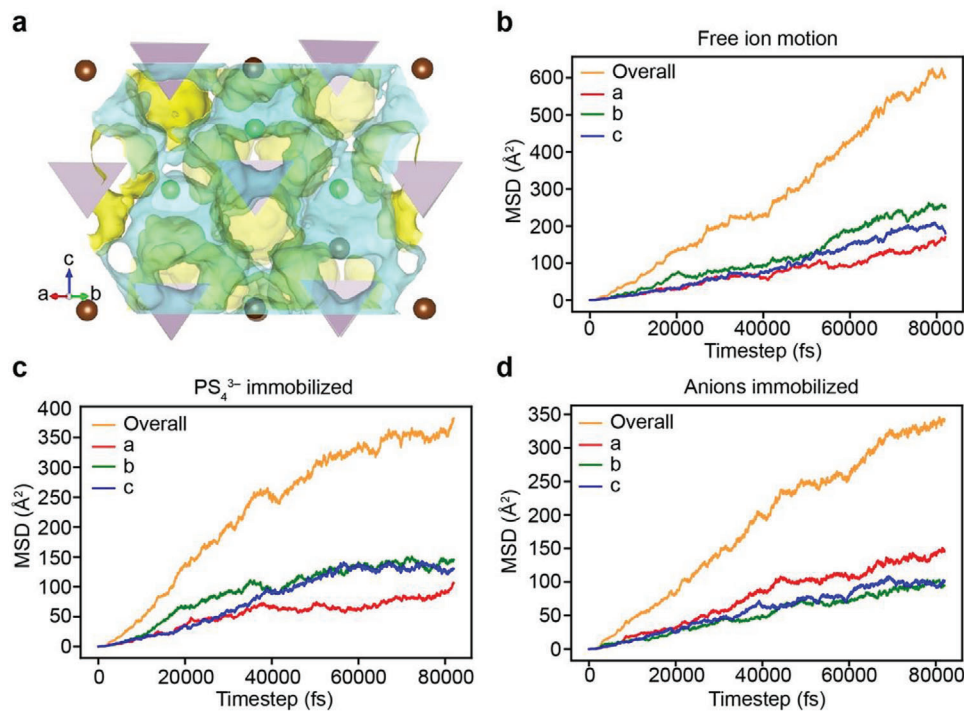


Figure 8. The effects of PS_4^{3-} motion on Li^+ -ion diffusion. a) Superimposed trajectories of Li (green) and S (yellow) in $\text{Li}_{5.25}\text{PS}_{4.25}\text{Cl}_{0.875}\text{Br}_{0.875}$ based on AIMD simulations. Mean square displacements (MSD) of Li in the $\text{Li}_{5.25}\text{PS}_{4.25}\text{Cl}_{0.875}\text{Br}_{0.875}$ structures with different dynamical constraints: b) no dynamical constraints; c) only PS_4^{3-} immobilized; d) all anions immobilized. The results reveal that PS_4^{3-} plays a key role in facilitating fast Li diffusion.

shaping the energy landscape. Our study offers valuable insights into the intricate structure-property relationships of high-entropy superionic conductors. Moreover, it illuminates the significance of lattice dynamics heterogeneity for ion transport, an area that has been considerably understudied.

4. Experimental Section

Synthesis: The powder with the corresponding stoichiometric ratio required for $\text{Li}_{5.3}\text{PS}_{4.3}\text{Cl}_{1.7-x}\text{Br}_x$ was prepared by mixing Li_2S (99.98%, Sigma-Aldrich), P_2S_5 (99%, Sigma-Aldrich), LiCl (99%, Sigma-Aldrich), and LiBr (99%, Sigma-Aldrich) using an agate mortar. Then, the hand-ground mixture was sealed in a 40 mL ZrO_2 jar and ball-milled for 30 min with a speed-fixed Spex mixer (two 12 mm ZrO_2 balls and ≈ 2 g powder were used). The as-milled powder was transferred to an air-tight quartz tube. The powder was fired at 300 °C for 12 h with a ramp of 1 °C min^{-1} in a box furnace (Thermo). The color of the powder turned light grey after sintering. The pretreated powder was hand-ground again and pressed into a 6 mm pellet with a thickness of around 1 mm using a stainless-steel mold. Finally, the pellet was sintered again at 450–460 °C for 12 h with a ramp of 1 °C min^{-1} under vacuum. All the steps mentioned above were conducted in an argon-filled glovebox (Mbraun) to avoid exposure to air. The same as-synthesized materials were used for diffraction, EIS, and solid-state NMR measurements described below.

X-Ray Powder Diffraction: Room-temperature X-ray powder diffraction measurements on $\text{Li}_{5.3}\text{PS}_{4.3}\text{Cl}_{1.7-x}\text{Br}_x$ were performed on a Rigaku Smartlab powder X-ray diffractometer using a copper source ($\lambda = 1.54$ Å). Powdered samples were finely packed into zero-background X-ray holders sealed with Kapton polyimide films to avoid exposure to air. Data acquisition was performed with 2θ changing from 10 to 120°. The acquisition time was around 1 h with a step size of 0.03° and a rotating speed of 2° min^{-1} . Structure analyses (unit cell and phase) on the X-ray Bragg diffractions of $\text{Li}_{5.3}\text{PS}_{4.3}\text{Cl}_{1.7-x}\text{Br}_x$ were accomplished using GSAS II software.^[36]

Neutron Diffraction: Room-temperature neutron total scattering experiments on the $\text{Li}_6\text{PS}_5\text{Cl}$, $\text{Li}_{5.7}\text{PS}_{4.7}\text{ClBr}_{0.3}$, and $\text{Li}_{5.5}\text{PS}_{4.5}\text{ClBr}_{0.5}$ were performed at the Spallation Neutron Source at Oak Ridge National Laboratory at the NOMAD beamline (BL-1B). The data collection was described by the previous studies.^[30] The MEM was employed to obtain the maps of the nuclear density distribution of Li-Argyrodites using the limited-memory BFGS algorithm (L-BFGS) in Dysnomia.^[37] The input file (.mem) was derived from Jana2006^[38] based on the refined crystal structure generated by TOPAS (v6).^[39] The Lagrangian multiplier was 0.001, and the number of voxels in the unit cell was $128 \times 128 \times 128$. The coefficients t and E (see Dysnomia's manual) were optimized to satisfy the constraints (central moments). The output file (.pgrid) was directly examined in VESTA^[40] without further processing.

Electrochemical Measurements: Room-temperature ionic conductivity was determined with EIS. AC impedance measurements were performed using Gamry Reference 600+ with a frequency range of 1 Hz to 5 MHz. The sintered pellets (6 mm in diameter and 1 mm in thickness) were used for the measurements. Indium foils were pressed onto both sides of the pellet as blocking electrodes. The sandwiched electrolyte pellet was then sealed in a cylindrical cell for measurements with an applied voltage of 10 mV. The temperature-dependent impedance measurements were conducted using a CSZ MicroClimate chamber. The temperature was changed with a step size of 20 °C within the range of 20–120 °C. The EIS spectra were measured 30 min after the set temperatures were reached.

Solid-State NMR Measurements: ^6Li and ^{31}P MAS NMR experiments were performed on a Bruker Avance III-500 spectrometer with a magnetic field of 11.75 T, which translates to the Larmor frequencies of 73.58 and 202.4 MHz for ^6Li and ^{31}P , respectively. The powdered electrolyte samples were packed tightly into 2.5 mm rotors spun at 25 kHz. The ^6Li spectra were collected with a $\pi/2$ pulse of 4.75 μs . The ^6Li shifts were referenced to $\text{LiCl}_{(\text{s})}$ at -1.1 ppm. For ^{31}P NMR, a rotor-synchronized spin-echo sequence of 4.2–8.4 μs ($\pi/2-\pi$) was used, and the ^{31}P shifts were referenced to 85% H_3PO_4 solution at 0 ppm. ^7Li and ^{31}P spin-lattice relaxation times (T_1) were measured using inversion recovery experiments with 9 and 14

increments of delays between the π and the $\pi/2$ pulses for ^7Li and ^{31}P , respectively.

^{35}Cl and ^{79}Br NMR experiments were carried out using a home-built probe in a 19.6 T superconductive magnet. The powdered samples were packed in 3.2 mm rotors that spun at 16 kHz. A 3QMAS spectrum of $\text{Li}_{5.3}\text{PS}_{4.3}\text{Cl}_{0.8}\text{Br}_{0.9}$ was acquired using an excitation and a conversion pulse of 7 and 3 μs , respectively. The length of the selective $\pi/2$ pulse was 20 μs . 2400 scans were acquired for each rotor-synchronized t_1 increment. The 1D spectra of $\text{Li}_{5.3}\text{PS}_{4.3}\text{Cl}_{1-x}\text{Br}_x$ were collected using a spin-echo pulse of 2.9–5.8 μs ($\pi/2-\pi$). The ^{35}Cl T_1 of $\text{Li}_{5.3}\text{PS}_{4.3}\text{Cl}_{0.8}\text{Br}_{0.9}$ was measured using a saturation recovery method. The 3QMAS spectrum was acquired with a recycle delay of 0.1 s and processed using the Q-shearing method^[41] to avoid peak aliasing. ^{79}Br QCPMG NMR experiments were performed under static conditions. The QCPMG sequence consists of an excitation pulse of 1.6 μs and a train of refocusing pulses of 3.2 μs . The duration of half echo was optimized to 0.15 ms. The ^{79}Br T_1 of $\text{Li}_{5.3}\text{PS}_{4.3}\text{Cl}_{0.8}\text{Br}_{0.9}$ was determined using a saturation recovery pulse integrated with a QCPMG sequence. All ^{35}Cl and ^{79}Br shifts were referenced to $\text{LiCl}_{(s)}$ and $\text{KBr}_{(s)}$ at 9.9 and 54.5 ppm, respectively.

Computational Approach: All density functional theory (DFT) energy calculations and AIMD simulations were carried out using the Vienna ab initio simulation package (VASP).^[42] The projector augmented wave (PAW) approach^[43] was used and Perdew–Burke–Ernzerhof generalized-gradient approximation (GGA-PBE) was chosen as the exchange–correlation functional.^[44] The VASP pseudopotential set of Li (PAW_PBE Li 17Jan2003), P (PAW_PBE P 17Jan2003), S (PAW_PBE S 17Jan2003), Br (PAW_PBE Br 06Sep2000), and Cl (PAW_PBE Cl 17Jan2003) was used. To optimize the structure of $\text{Li}_{5.25}\text{PS}_{4.25}\text{Cl}_{0.875}\text{Br}_{0.875}$, Python Materials Genomics (pymatgen) package^[45] was adopted. 20 $\text{Li}_{42}\text{P}_8\text{S}_{34}\text{Cl}_8\text{Br}_8$ supercells with different structures were generated based on the $2 \times 1 \times 1$ supercell of $\text{Li}_6\text{PS}_5\text{Br}$ from the Materials Project^[46] (ID: mp-985591). Atom coordinates and unit cell parameters were then optimized using DFT calculations. The final structure with the lowest total energy was obtained with $a = 19.915 \text{ \AA}$, $b = 9.938 \text{ \AA}$, $c = 10.076 \text{ \AA}$, and $\alpha = \beta = \gamma = 90^\circ$. All the other parameters used for geometry optimization were kept the same as the default in Pymatgen, with a grid density of 787 atom⁻¹. The structure of $\text{Li}_6\text{PS}_5\text{Cl}$ was acquired from the Materials Project (ID: mp-985592). The AIMD simulations^[47] were performed based on the canonical ensemble for at least 80 ps with a step size of 2 fs. The temperature ramp starting from 100 K to the desired value was finished in the first 2 ps. In order to examine the motional correlation between different atoms, some atoms were immobilized by applying dynamical constraints.

Supporting Information

Supporting Information is available from the Wiley Online Library or from the author.

Acknowledgements

P.W. and S.P. contributed equally to this work. The authors acknowledge the support from the National Science Foundation under grant no. DMR-1847038 and from the NSF MRSEC program (NSF DMR-1720139). All solid-state NMR experiments were performed at the National High Magnetic Field Laboratory. The National High Magnetic Field Laboratory is supported by the National Science Foundation through NSF/DMR-1644779 and the State of Florida. A portion of this research used resources at the Spallation Neutron Source, a DOE Office of Science User Facility operated by the Oak Ridge National Laboratory. The authors thank Dr. Zhe-hong Gan for the helpful discussion on the processing and analysis of the 3QMAS ^{35}Cl NMR.

Conflict of Interest

The authors declare no conflict of interest.

Data Availability Statement

The data that support the findings of this study are available in the supplementary material of this article.

Keywords

high entropy, lattice dynamics, mixed anion, solid-state nuclear magnetic resonance, superionic conductors

Received: July 27, 2023
Published online: August 31, 2023

- [1] J. Janek, W. G. Zeier, *Nat. Energy* **2016**, *1*, 16141.
- [2] M. Li, C. Wang, Z. Chen, K. Xu, J. Lu, *Chem. Rev.* **2020**, *120*, 6783.
- [3] Y. Kato, S. Hori, T. Saito, K. Suzuki, M. Hirayama, A. Mitsui, M. Yonemura, H. Iba, R. Kanno, *Nat. Energy* **2016**, *1*, 16030.
- [4] A. Hayashi, N. Masuzawa, S. Yubuchi, F. Tsuji, C. Hotehama, A. Sakuda, M. Tatsumisago, *Nat. Commun.* **2019**, *10*, 5266.
- [5] T. Fuchs, S. P. Culver, P. Till, W. G. Zeier, *ACS Energy Lett.* **2020**, *5*, 146.
- [6] X. Feng, P.-H. Chien, Z. Zhu, I.-H. Chu, P. Wang, M. Immediato-Scuotto, H. Arabzadeh, S. P. Ong, Y.-Y. Hu, *Adv. Funct. Mater.* **2019**, *29*, 1807951.
- [7] P. Wang, H. Liu, S. Patel, X. Feng, P.-H. Chien, Y. Wang, Y.-Y. Hu, *Chem. Mater.* **2020**, *32*, 3833.
- [8] X. Feng, P.-H. Chien, Y. Wang, S. Patel, P. Wang, H. Liu, M. Immediato-Scuotto, Y.-Y. Hu, *Energy Storage Mater.* **2020**, *30*, 67.
- [9] P. Adeli, J. D. Bazak, K. H. Park, I. Kochetkov, A. Huq, G. R. Goward, L. F. Nazar, *Angew. Chem., Int. Ed.* **2019**, *58*, 8681.
- [10] A. Gautam, M. Sadowski, M. Ghidui, N. Minafra, A. Senyshyn, K. Albe, W. G. Zeier, *Adv. Energy Mater.* **2020**, *11*, 2003369.
- [11] P. Adeli, J. D. Bazak, A. Huq, G. R. Goward, L. F. Nazar, *Chem. Mater.* **2021**, *33*, 146.
- [12] M. Brinek, C. Hiebl, H. M. R. Wilkening, *Chem. Mater.* **2020**, *32*, 4754.
- [13] T. K. Schwieter, V. A. Arszewska, C. Wang, C. Yu, A. Vasileiadis, N. J. J. de Klerk, J. Hageman, T. Hupfer, I. Kerkamm, Y. Xu, E. van der Maas, E. M. Kelder, S. Ganapathy, M. Wagemaker, *Nat. Mater.* **2020**, *19*, 428.
- [14] I. Hanghofer, B. Gadermaier, H. M. R. Wilkening, *Chem. Mater.* **2019**, *31*, 4591.
- [15] M. A. Kraft, S. P. Culver, M. Calderon, F. Böcher, T. Krauskopf, A. Senyshyn, C. Dietrich, A. Zevkink, J. Janek, W. G. Zeier, *J. Am. Chem. Soc.* **2017**, *139*, 10909.
- [16] M. A. Kraft, S. Ohno, T. Zinkevich, R. Koerver, S. P. Culver, T. Fuchs, A. Senyshyn, S. Indris, B. J. Morgan, W. G. Zeier, *J. Am. Chem. Soc.* **2018**, *140*, 16330.
- [17] H.-J. Deiseroth, S.-T. Kong, H. Eckert, J. Vannahme, C. Reiner, T. Zaiß, M. Schlosser, *Angew. Chem., Int. Ed.* **2008**, *47*, 755.
- [18] P. R. Rayavarapu, N. Sharma, V. K. Peterson, S. Adams, *J. Solid State Electrochem.* **2012**, *16*, 1807.
- [19] N. Minafra, M. A. Kraft, T. Berges, C. Li, R. Schlem, B. J. Morgan, W. G. Zeier, *Inorg. Chem.* **2020**, *59*, 11009.
- [20] N. J. J. de Klerk, I. Rosłoń, M. Wagemaker, *Chem. Mater.* **2016**, *28*, 7955.
- [21] W. Huang, K. Yoshino, S. Hori, K. Suzuki, M. Yonemura, M. Hirayama, R. Kanno, *J. Solid State Chem.* **2019**, *270*, 487.
- [22] W. Huang, L. Cheng, S. Hori, K. Suzuki, M. Yonemura, M. Hirayama, R. Kanno, *Mater. Adv.* **2020**, *1*, 334.
- [23] S. Ohno, B. Helm, T. Fuchs, G. Dewald, M. A. Kraft, S. P. Culver, A. Senyshyn, W. G. Zeier, *Chem. Mater.* **2019**, *31*, 4936.

- [24] Y. B. Song, D. H. Kim, H. Kwak, D. Han, S. Kang, J. H. Lee, S.-M. Bak, K.-W. Nam, H.-W. Lee, Y. S. Jung, *Nano Lett.* **2020**, *20*, 4337.
- [25] F. Zhao, J. Liang, C. Yu, Q. Sun, X. Li, K. Adair, C. Wang, Y. Zhao, S. Zhang, W. Li, S. Deng, R. Li, Y. Huang, H. Huang, L. Zhang, S. Zhao, S. Lu, X. Sun, *Adv. Energy Mater.* **2020**, *10*, 1903422.
- [26] L. Zhou, A. Assoud, Q. Zhang, X. Wu, L. F. Nazar, *J. Am. Chem. Soc.* **2019**, *141*, 19002.
- [27] T. Bernges, S. P. Culver, N. Minafra, R. Koerver, W. G. Zeier, *Inorg. Chem.* **2018**, *57*, 13920.
- [28] R. Schlem, M. Ghidui, S. P. Culver, A.-L. Hansen, W. G. Zeier, *ACS Appl. Energy Mater.* **2020**, *3*, 9.
- [29] H. M. Chen, C. Maohua, S. Adams, *Phys. Chem. Chem. Phys.* **2015**, *17*, 16494.
- [30] S. V. Patel, S. Banerjee, H. Liu, P. Wang, P.-H. Chien, X. Feng, J. Liu, S. P. Ong, Y.-Y. Hu, *Chem. Mater.* **2021**, *33*, 1435.
- [31] J. Lin, G. Cherkashinin, M. Schäfer, G. Melinte, S. Indris, A. Kondrakov, J. Janek, T. Brezesinski, *ACS Mater. Lett.* **2022**, *4*, 2187.
- [32] F. Strauss, J. Lin, A. Kondrakov, T. Brezesinski, *Matter.* **2023**, *6*, 1068.
- [33] F. Strauss, J. Lin, M. Duffiet, K. Wang, T. Zinkevich, A.-L. Hansen, S. Indris, T. Brezesinski, *ACS Mater. Lett.* **2022**, *4*, 418.
- [34] L. Frydman, J. S. Harwood, *J. Am. Chem. Soc.* **1995**, *117*, 5367.
- [35] J.-B. d'Espinose de Lacaillerie, C. Fretigny, D. Massiot, *J. Magn. Reson.* **2008**, *192*, 244.
- [36] B. H. Toby, R. B. Von Dreele, *J. Appl. Crystallogr.* **2013**, *46*, 544.
- [37] K. Momma, T. Ikeda, A. A. Belik, F. D. Izumi, *Powder Diffr.* **2013**, *28*, 184.
- [38] V. Petříček, M. Dušek, L. Palatinus, *Z. Kristallogr. Cryst. Mater.* **2014**, *229*, 345.
- [39] A. A. Coelho, *J. Appl. Crystallogr.* **2018**, *51*, 210.
- [40] K. Momma, F. Izumi, *J. Appl. Crystallogr.* **2008**, *41*, 653.
- [41] I. Hung, J. Trébosc, G. L. Hoatson, R. L. Vold, J.-P. Amoureux, Z. Gan, *J. Magn. Reson.* **2009**, *201*, 81.
- [42] G. Kresse, J. Furthmüller, *Phys. Rev. B* **1996**, *54*, 11169.
- [43] P. E. Blöchl, *Phys. Rev. B* **1994**, *50*, 17953.
- [44] J. P. Perdew, K. Burke, M. Ernzerhof, *Phys. Rev. Lett.* **1996**, *77*, 3865.
- [45] S. P. Ong, W. D. Richards, A. Jain, G. Hautier, M. Kocher, S. Cholia, D. Gunter, V. L. Chevrier, K. A. Persson, G. Ceder, *Comput. Mater. Sci.* **2013**, *68*, 314.
- [46] A. Jain, S. P. Ong, G. Hautier, W. Chen, W. D. Richards, S. Dacek, S. Cholia, D. Gunter, D. Skinner, G. Ceder, K. A. Persson, *APL Mater.* **2013**, *1*, 011002.
- [47] Y. Wang, W. D. Richards, S. P. Ong, L. J. Miara, J. C. Kim, Y. Mo, G. Ceder, *Nat. Mater.* **2015**, *14*, 1026.